Journal of Materials Chemistry A

ROYAL SOCIETY OF CHEMISTRY

PAPER

View Article Online
View Journal | View Issue

Published on 11 December 2021. Downloaded by Soochow University China on 3/12/2022 11:49:42 AM.

Check for updates

Cite this: *J. Mater. Chem. A*, 2022, **10**, 1891

Rh/RhO_x nanosheets as pH-universal bifunctional catalysts for hydrazine oxidation and hydrogen evolution reactions†

Junjun Yang,‡[a] Liang Xu,‡[a] Wenxiang Zhu,[a] Miao Xie,[a] Fan Liao, *[a] Tao Cheng, *[a] Zhenhui Kang [ab] and Mingwang Shao *[a]

Received 2nd November 2021
Accepted 10th December 2021

DOI: 10.1039/d1ta09391f

rsc.li/materials-a

Hydrazine oxidation reaction (HzOR)-assisted hydrogen evolution is a promising effluent treatment and energy conversion method for resolving the global energy shortage and environmental crisis. However, highly efficient and pH-universal electrocatalysts are still lacking to boost the sluggish kinetics of both the cathodic hydrogen evolution reaction (HER) and anodic HzOR. Here, Rh/RhO_x nanosheets with Rh–O–Rh interfaces are fabricated by alkali-assisted synthesis and the H_2 reduction route. When they are employed as efficient bifunctional electrocatalysts, the Rh/RhO_x nanosheets exhibit outstanding performance and stability for the HER and HzOR in pH-universal electrolytes. The two-electrode electrolyzer delivers a current density of 10 mA cm^{-2} with an ultra-low voltage of 0.068, 0.268, and 0.348 V in 1.0 M KOH/0.5 M N_2H_4, 1.0 M PBS/0.3 M N_2H_4 and 0.5 M H_2SO_4/0.5 M N_2H_4, respectively. The performance can be maintained over 65 h for the HER and HzOR under neutral conditions. Density functional theory calculations indicate that the high activity is derived from the Rh–O–Rh interfaces. The regulation of the interface greatly improves the activity of the catalyst and reduces energy consumption, which is more conducive to the production of hydrogen.

Introduction

Hydrogen (H_2) is an efficient and clean energy carrier to solve the energy crisis and environmental problems caused by the use of fossil fuels.[1–3] Electrocatalytic water decomposition is one of the most ecofriendly pathways to produce H_2. However, the overall water splitting (OWS) system is adversely affected by the anodic reaction, the oxygen evolution reaction (OER), which has a high thermodynamic potential of 1.23 V *vs.* RHE.[4,5] Replacing water oxidation with other chemical oxidation reactions is an effective strategy to decrease cell voltages. Similar to the traditional electrolytic water hydrogen production, small molecule oxidation-assisted water electrolysis retains the traditional cathodic HER reaction and uses substances with more thermodynamic advantages for the oxidation reaction at the anode, which greatly reduces the voltage required for electrolytic hydrogen production, such as the formic acid oxidation reaction,[6] ethanol oxidation reaction,[7] ammonia electrooxidation reaction,[8] hydrazine oxidation reaction (HzOR)[9,10] and so on. Among the many options, the hydrazine oxidation reaction with a theoretical potential value of −0.33 V *vs.* RHE is an attractive one to couple with the cathodic HER and enhance the overall electrolytic efficiency for H_2 production.[11–13] Furthermore, the byproduct when using a hydrazine-assisted electrolyzer is only N_2 without any carbon emission, which is safe and environmentally friendly compared with OWS and other chemical-assisted electrolyzers.[14,15]

The following question is to find proper catalysts for overall hydrazine splitting (OHzS). Hydrazine is widely used in the chemical industry, medicine, agricultural products, water treatment and many other industrial fields, and is always present in industrial wastewater.[16] Wastewater containing hydrazine is toxic and mutagenic and should be treated to meet national discharge standards.[17] So designing catalysts with high activity and adaptation to a variety of electrolytic environments is challenging but attractive for OHzS and wastewater treatment.

Rhodium is a well-known noble metal, and it shows high catalytic activity towards many important industrial processes. However, there are few reports on its application in hydrazine oxidation.[5,12,18] In order to further improve the performance, some explorations were carried out by adjusting the morphology and interface, which are important factors to realize the modulations of the active sites and electronic structure of the catalysts. Some inspiring pioneering studies

[a]*Institute of Functional Nano & Soft Materials (FUNSOM), Jiangsu Key Laboratory for Carbon-Based Functional Materials & Devices, Soochow University, Suzhou 215123, P. R. China. E-mail: fliao@suda.edu.cn; tcheng@suda.edu.cn; mwshao@suda.edu.cn*

[b]*Macau Institute of Materials Science and Engineering, Macau University of Science and Technology, Macau, China*

† Electronic supplementary information (ESI) available: Experimental data, electrochemical measurements, and computational details. See DOI: 10.1039/d1ta09391f

‡ J. J. Yang and L. Xu contributed equally.

Published on 11 December 2021. Downloaded by Soochow University China on 3/12/2022 11:49:42 AM.

have been performed accordingly.[19–21] For example, Liu *et al.* fabricated an ultra-thin Ni_3S_2 nanosheet array on the nickel foam substrate, which was employed as the anode and cathode in a double electrode system.[22] The nanosheet structure is helpful to increase the specific surface area and expose the active site. Different compositions of the catalysts establish interfaces, which improve the intrinsic catalytic activities through the interfacial synergy effect. Kundu *et al.* designed and synthesized Rh–Rh_2O_3 nanocomposites with nitrogen-doped carbon.[23] The presence of Rh_2O_3 increases the HER activity of the catalyst by 10 times compared with the catalyst without oxide in the same electrolyte. The synergistic effect of Rh metal and the Rh_2O_3 interface for H adsorption and OH^- adsorption respectively is the main determinant to enhance the activity of the catalyst. Puigdollers *et al.* also demonstrated that the oxygen atoms in the boundary region between metal and oxide have particularly high reactivity. The regulation of the metal/oxide interface plays an indispensable role in the field of catalysis.[24]

Inspired by these studies, here Rh/RhO_x nanosheets are fabricated as a bifunctional catalyst for both the HER and HzOR under all pH conditions. By a strong alkali-assisted thermo-synthesis and the following H_2 reduction treatment, small Rh nanoparticles are *in situ* grown on RhO_x nanosheets, offering tight interfacial interaction between the metal and oxide, leading to the adjusted chemical state of Rh. The optimal Rh/RhO_x-500 catalyst exhibits excellent performance for the HER and HzOR under all pH conditions and is superior to Pt/C and most of the current HER and HzOR catalysts. When fabricating the water splitting device, the OHzS system only requires the cell voltages of 0.068, 0.268, and 0.348 V for a current density of 10 mA cm^{-2} in 1.0 M KOH, 1.0 M PBS, and 0.5 M H_2SO_4 electrolytes with a certain amount of N_2H_4. Additionally, the Rh/RhO_x-500 catalyst also exhibits remarkable stability. The density functional theory (DFT) calculations indicate that the introduction of the interface of Rh/RhO_x activates the surface Rh and reduces the energy barrier of the reaction, leading to the excellent performance of the Rh/RhO_x-500 catalyst.

Results and discussion

Characterization of Rh/RhO_x nanosheets

The fabrication of Rh/RhO_x-500 is divided into two steps as shown in the synthetic scheme (Fig. S1 and ESI†). The precursor of RhO_x-500 nanosheets was synthesized by evaporating a mixture of $RhCl_3 \cdot 3H_2O$ and high concentration KOH (6 M), and then calcining at 500 °C. The scanning electron microscopy (SEM) image and transmission electron microscopy (TEM) image of RhO_x-500 are shown in Fig. 1a and S2.† The morphology of RhO_x-500 is a rigid lamellar structure. As can be seen from Fig. 1a and S3,† the diameter of RhO_x-500 ranges from 100 to 500 nm and the thickness is about 50 nm. The X-ray diffraction pattern of RhO_x-500 is shown in Fig. 1d. The obtained XRD peaks at 12.8°, 25.9°, and 36.5° show the proportionate *d* values for RhO_x-500, indicating the layered structure of RhO_x.[25] The morphology of the precursors calcined at different temperatures (300–600 °C) is also compared and shown in Fig. S4.† RhO_x-300 has no special morphology. Although RhO_x-400 and RhO_x-600 also show layered structures, their morphology is not uniform. The XRD patterns of the RhO_x precursors at different calcination temperatures were recorded and shown in Fig. S5.† The most obvious peaks for the layered structure appear at about 500 °C, from which can it can be inferred that RhO_x-500 has the best layered structure compared to the samples obtained at other temperatures. In addition, more experiments with different precursors were conducted. The corresponding characterization results are shown in Fig. S6.† When KCl was used as the raw material, irregular blocks were obtained (Fig. S6b†). When NaOH was used as the raw material, only RhO_x nanoparticles were obtained (Fig. S6d†). The XRD patterns of these two samples do not show the layered structures (Fig. S6a and c†). These results suggested that the selection of different precursors will change the crystal structure and morphology of RhO_x.

Then Rh/RhO_x-500 is obtained by an Ar/H_2 reduction method, which still retains the nanosheet morphology with small nanoparticles on the surface of the nanosheets (Fig. 1b and c). In addition, the TEM image (Fig. 1c) showed that there are obvious voids on the RhO_x nanosheet after Ar/H_2 reduction, which increases the specific surface area and exposes more active sites. The XRD pattern of Rh/RhO_x-500 (Fig. 1d) proves the formation of Rh, in which the diffraction peaks are well indexed to the (111), (200), (220), and (311) planes face-centered cubic Rh (JCPDS no. 05-0685). The Rh particles are circled in yellow in the high magnification TEM image of Rh/RhO_x-500 (Fig. 1e), with the size calculated to be about 11.9 nm according to the Scherrer formula.[26] The detailed calculation process is shown in Fig. S7.† In the high-resolution transmission electron microscope (HRTEM) image of Rh/RhO_x-500 (Fig. 1f), the lattice fringes with a spacing of 0.219 nm can be indexed to the (111) crystal face of face-centered cubic Rh. The lattice fringes with a spacing of 0.190 nm can be indexed to the (200) crystal face of Rh. The angle between the two crystal faces is 54.7°. Moreover, the good distribution of Rh and O elements in Rh/RhO_x-500 was also revealed by the HAADF-STEM image and corresponding elemental mapping distributions (Fig. 1g).

The electronic states of RhO_x-500, Rh/RhO_x-300, and Rh/RhO_x-500 were investigated using X-ray photo electron spectroscopy (XPS). The co-existence of C, O, and Rh elements in RhO_x-500, Rh/RhO_x-300, and Rh/RhO_x-500 can be clearly identified by comparing the full XPS spectra (Fig. S8a†). In the high-resolution spectra of O 1s for RhO_x-500 and Rh/RhO_x-500 (Fig. S8b and c†), the peaks at 530.1 and 532.1 eV are ascribed to the C=O/C–O and lattice O, respectively.[27] Meanwhile, the Rh 3d spectra of RhO_x-500, Rh/RhO_x-300, and Rh/RhO_x-500 are exhibited in Fig. 1h, i, and S7d.† For Rh/RhO_x-500, the peaks located at 307.2 and 311.9 eV are attributed to Rh^0, those at 308.5 and 313.2 eV to Rh^{3+}, and those at 309.4 eV and 314.1 eV to Rh^{4+}, respectively. The above high solution Rh spectra suggest the formation of metallic Rh after heating at 200 °C under the condition of Ar/H_2. Compared with the literature reports, the binding energy of metallic Rh in Rh/RhO_x-500 shifted to higher energy by about 0.2 eV, which may be due to the strong electronic interaction between RhO_x and Rh.[28–32] In addition, 70%

 This journal is © The Royal Society of Chemistry 2022

Published on 11 December 2021. Downloaded by Soochow University China on 3/12/2022 11:49:42 AM.

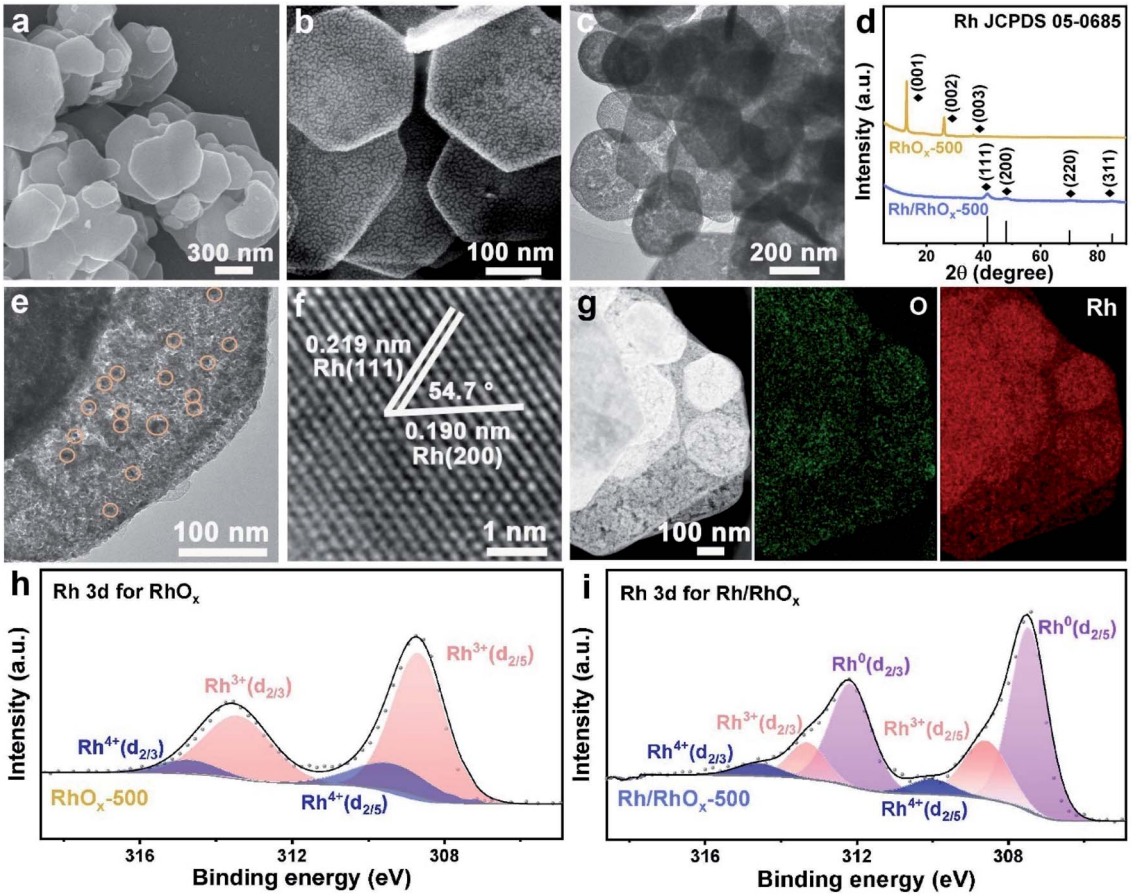

Fig. 1 (a) and (b) SEM images of RhO_x-500 and Rh/RhO_x-500. (c) TEM image of Rh/RhO_x-500. (d) XRD patterns of RhO_x-500 and Rh/RhO_x-500. (e) TEM image at high magnification and (f) HRTEM image of Rh/RhO_x-500. (g) HAADF-STEM image and corresponding elemental mapping of Rh/RhO_x-500. (h) and (i) XPS spectra of Rh 3d for RhO_x-500 and Rh/RhO_x-500.

wt of RhO_x was reduced to Rh according to the peak ratio of RhO_x and Rh for Rh/RhO_x-500.

HzOR activity of Rh/RhO_x-500 in electrolytes with different pH values

Inspired by the unique structure of Rh/RhO_x-500, its electrocatalytic activity towards the HzOR is evaluated and compared with other samples in different electrolytes including 1.0 M KOH, 1.0 M PBS, and 0.5 M H_2SO_4, respectively. Among the three electrolytes, we focused on neutral solutions from the perspectives of environmental protection and practicality, which is also a challenging condition for the catalysts compared with those tested in acidic or basic media.[33–35] The tests were performed at a scanning rate of 5 mV s^{-1} in a typical three-electrode system. The catalytic activity of Rh/RhO_x-500 for the HzOR in a neutral medium is shown in Fig. 2a. There is no obvious anodic response current in the potential window without adding N_2H_4, but with the increased concentration of hydrazine, the anodic response current increases sharply, and the best performance is observed in 1.0 M PBS/0.3 M N_2H_4 electrolyte. When the concentration of hydrazine is above 0.3 M, the corresponding current densities tend to be the same. Thus, the catalysts are compared in 1.0 M PBS/0.3 M N_2H_4 electrolyte for the HzOR. By comparing the LSV curves of Rh/RhO_x-500 in different hydrazine concentrations (Fig. S9†), electrochemical tests were carried out in 1.0 M KOH/0.5 M N_2H_4 electrolyte and 0.5 M H_2SO_4/0.5 M N_2H_4 electrolyte in alkaline and acidic environments for the HzOR. Moreover, the LSV curves for the HzOR by Rh/RhO_x at different calcination temperatures indicate that the best sample is obtained at 500 °C (Fig. S10†). After adjusting the treatment time and temperature of Ar/H_2, it was found that the best sample for the HzOR was obtained at the treatment temperature of 200 °C and the reaction time of 1 h (Fig. S11†). Rh/RhO_x-500 provides a current density of 10 mA cm^{-2} at a low potential of 94 mV *vs.* RHE. In contrast, RhO_x-500, Rh/RhO_x-300, and Pt/C require 536, 165, and 138 mV *vs.* RHE to provide the same current density, respectively (Fig. 2b), suggesting the significantly improved HzOR activity of Rh/RhO_x-500.

The corresponding Tafel slope (Fig. 2c) of Rh/RhO_x-500 in 1.0 M PBS/0.3 M N_2H_4 is 63.6 mV dec^{-1}, much lower than those of Rh/RhO_x-300 (118.6 mV dec^{-1}) and Pt/C (101.4 mV dec^{-1}), which indicates its faster HzOR kinetics. Comparing Rh/RhO_x-500 and Rh/C, obviously the potential of Rh/C for the HzOR is larger than that of Rh/RhO_x-500 (Fig. S12†), demonstrating that

Published on 11 December 2021. Downloaded by Soochow University China on 3/12/2022 11:49:42 AM.

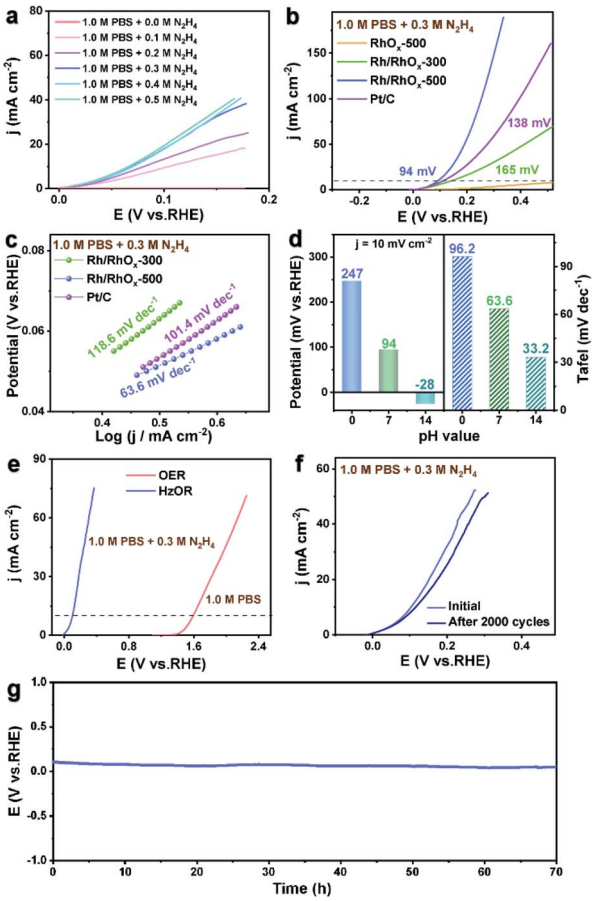

Fig. 2 (a) LSV curves of Rh/RhO$_x$-500 toward different concentrations of hydrazine in 1.0 M PBS. (b) LSV curves of different catalysts in 1.0 M PBS/0.3 M N_2H_4. (c) Corresponding Tafel plots derived from (a). (d) Comparison of potential to drive a current density of 10 mA cm^{-2} and Tafel plots of Rh/RhO$_x$-500 for the HzOR in different pH solutions. (e) LSV curves for the HzOR and OER. (f) LSV curves of Rh/RhO$_x$-500 before and after 2000 CV cycles. (g) The chronopotentiometric stability of Rh/RhO$_x$-500 recorded at 10 mA cm^{-2} current density.

the performance of Rh/C alone is inferior to that of Rh/RhO$_x$-500. In both acidic (0.5 M H_2SO_4) and alkaline (1.0 M KOH) solutions (Fig. S13†), the catalytic and kinetic performances of Rh/RhO$_x$-500 are better than those of Rh/RhO$_x$-300 and Pt/C. Especially, Rh/RhO$_x$-500 only needs −28 mV to reach 10 mA cm^{-2} in 1.0 M KOH/0.5 M N_2H_4. And the potential to drive a current density of 10 mA cm^{-2} and Tafel plots of Rh/RhO$_x$-500 for the HzOR in different pH solutions are summarized in Fig. 2d.

Rh/RhO$_x$-500 also shows obvious advantages compared with other catalysts reported in the literature for the HzOR, with specific data recorded in Table S1.† Moreover, the comparison of LSV curves of the HzOR and OER demonstrates the great dynamic advantage of HzOR electrolysis (Fig. 2e). Only a potential of 94 mV *vs.* RHE is needed for the HzOR to achieve a current density of 10 mV cm^{-2} in 1.0 M PBS/0.3 M N_2H_4, while the OER needs a higher value of 1.53 V *vs.* RHE without adding N_2H_4. The same is true for the comparison of the HzOR and OER in alkaline and acidic electrolytes (Fig. S14†). In addition, Rh/RhO$_x$-500 exhibits outstanding stability for the HzOR, which is verified in Fig. 2f and g. The current density in the LSV curve after 2000 continuous cycles of CV scanning is almost unchanged as compared with the initial curve. Then in the chronopotentiometry test, the potential attenuation of Rh/RhO$_x$-500 is not obvious when it is tested at a constant current density of 10 mA cm^{-2} for more than 70 h. Rh/RhO$_x$-500 also showed great stability, which is better than that of Pt/C in alkaline and acidic electrolytes (Fig. S15†). The TEM image, XRD pattern, and XPS spectra of Rh/RhO$_x$-500 after 2000 CV cycles in 1.0 M PBS/0.3 M N_2H_4 are shown in Fig. S16.† Compared with the sample before the electrochemical test, the morphology of the nanosheet is well preserved, representing strong electrochemical stability. According to the XPS spectrum of Rh 3d (Fig. S16d†), the proportion of Rh^0 does not change obviously, verifying the stability of Rh/RhO$_x$-500.

HER activity of Rh/RhO$_x$-500 in electrolytes with different pH values

The performance of Rh/RhO$_x$-500 for the HER was also explored in 1.0 M KOH, 1.0 M PBS, and 0.5 M H_2SO_4, respectively. The electrocatalytic performances of Rh/RhO$_x$ prepared at different calcination temperatures (Fig. S17†) are compared first, where the best sample can be obtained by calcinating the raw materials for 2 h at 500 °C. Meanwhile, the sample obtained at this temperature also showed the best lamellar characteristic peaks in XRD characterization (Fig. S5†). The effect of Ar/H_2 treatment is investigated and the best performance of Rh/RhO$_x$-500 for the HER is still obtained at 200 °C for 1 h (Fig. S18†). Fig. 3a compares the linear sweep voltammetry (LSV) curves of RhO$_x$-500, Rh/RhO$_x$-300, Rh/RhO$_x$-500, and Pt/C in 1.0 M PBS. Rh/RhO$_x$-500 exhibits the best HER performance and requires an overpotential of 39 mV to deliver a current density of 10 mA cm^{-2}, which is obviously better than those of RhO$_x$-500 (419 mV), Rh/RhO$_x$-300 (185 mV), and Pt/C (47 mV). RhO$_x$-500 has a poor activity for the HER as indicated by the large overpotential and small current density, which proves that the main catalytically active species is Rh nanoparticles. The catalytic reaction kinetics of the HER was studied using the Tafel equation and the linear part of the Tafel curve was extracted to calculate the Tafel slope. As shown in Fig. 3b, the Tafel slope of Rh/RhO$_x$-500 is as low as 35.9 mV dec^{-1}, which is much smaller than that of other catalysts, indicating its excellent dynamic performance. In addition, LSV curves of Rh/RhO$_x$-500 and Rh/C in 1.0 M PBS for HER are provided (Fig. S19†), proving that the performance of Rh/C alone cannot do better than Rh/RhO$_x$-500.

The electrochemical active surface area (ECSA) is often reflected by the electrochemical double-layer capacitance (C_{dl}).[36] In Fig. 3c, the C_{dl} of Rh/RhO$_x$-500 is 26.6 mF cm^{-2}, which is evidently higher than those of Rh/RhO$_x$-300 (14.3 mF cm^{-2}) and Pt/C (20.0 mF cm^{-2}) as calculated based on the corresponding CV curves (Fig. S20†). Besides, based on their CV curves in 0.5 M H_2SO_4 solution in Fig. S21,† the ECSAs of Rh/RhO$_x$-300, Rh/RhO$_x$-500, and Pt/C were calculated. The ECSA of Rh/RhO$_x$-500 is 83.68 m^2 g^{-1}, which is 3.5- and 1.6-fold higher than those of Rh/RhO$_x$-300 (23.64 m^2 g^{-1}) and Pt/C (51.82 m^2 g^{-1}),

 This journal is © The Royal Society of Chemistry 2022

Published on 11 December 2021. Downloaded by Soochow University China on 3/12/2022 11:49:42 AM.

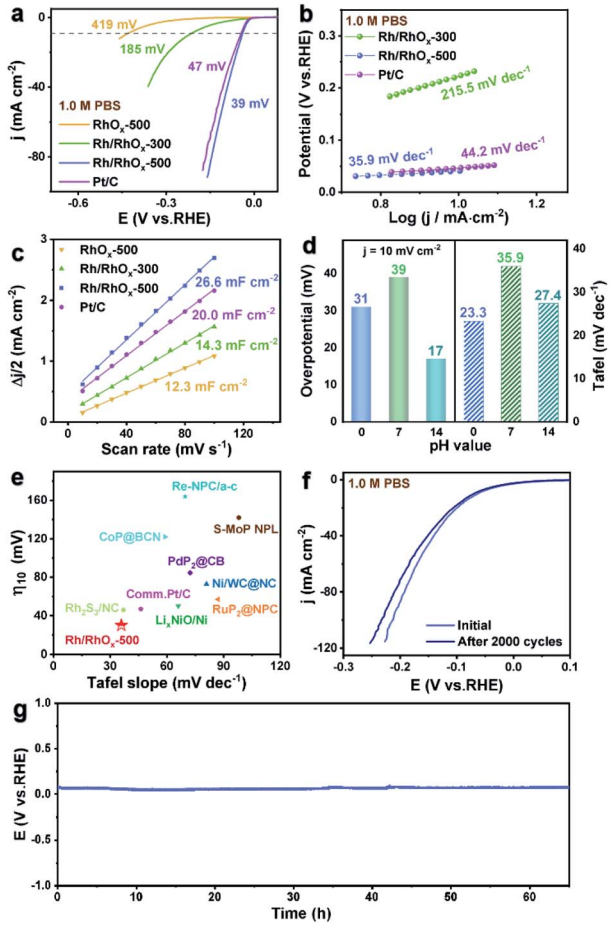

Fig. 3 (a) LSV curves of different catalysts in 1.0 M PBS. (b) Corresponding Tafel plots derived from (a). (c) C_{dl} values at a potential of 0.1 V *vs.* RHE. (d) Comparison of overpotential to drive a current density of 10 mA cm^{-2} and Tafel plots of Rh/RhO$_x$-500 for the HER in different pH solutions. (e) Comparison of overpotential @ 10 mA cm^{-2} and Tafel slopes for various HER catalysts in 1.0 M PBS. (f) LSV curves of Rh/RhO$_x$-500 before and after 2000 CV cycles. (g) The chronopotentiometric stability of Rh/RhO$_x$-500 recorded at 10 mA cm^{-2} current density.

respectively. Moreover, the specific surface areas of the catalysts are evaluated by the Brunauer–Emmett–Teller (BET) method in Fig. S22.† The BET surface area of Rh/RhO$_x$-500 (48.4 m^2 g^{-1}) is much larger than that of RhO$_x$-500. These data indicate the nanosheet structure of Rh/RhO$_x$-500 may provide a larger surface area and more active sites for catalysis. What is more, in order to further explain the high catalytic activity, the electrode dynamics in the HER were characterized by electrochemical impedance spectroscopy (EIS) in Fig. S23.† The impedance spectra were fitted using the model (inset in Fig. S23†) 2TS (R_s – (R_1||CPE$_1$) – (R_{ct}||CPE$_{int}$)), where R_s is the resistance of solution, R_{ct} is the resistance of charge transfer, and R_1 is the resistance of pores related to porosity.[37] It is known that electrocatalytic dynamics are reflected by R_{ct} and a lower R_{ct} value means a faster reaction rate.[38] The results show that the Rh/RhO$_x$-500 electrode has a lower charge transfer resistance in all pH solutions, which means the Rh/RhO$_x$-500 electrode is favorable for rapid interfacial charge transfer and electrochemical catalysis.

Additionally, Rh/RhO$_x$-500 also shows excellent HER performance in acidic and alkaline solutions. The values of overpotential at 10 mA cm^{-2} and Tafel slope for the HER are summarized in Fig. 3d, and the specific results in 1.0 M KOH and 0.5 M H_2SO_4 are shown in Fig. S24.† Rh/RhO$_x$-500 only needs 17 mV to reach 10 mA cm^{-2} and its overpotential and kinetic properties greatly surpass those of Pt/C in 1.0 M KOH (Fig. S24a–c†). In 0.5 M H_2SO_4 solution (Fig. S24d–f†), the overpotential of Rh/RhO$_x$-500 for driving a current density of 10 mA cm^{-2} is 31 mV, and the activity is higher than that of Pt/C when the potential exceeds 60 mV *vs.* RHE. The Tafel slope of Rh/RhO$_x$-500 is found to be 23.3 mV dec^{-1}, showing its excellent dynamic properties better than those of Pt/C (29.1 mV dec^{-1}), which is why it can exceed the current density of Pt/C at a high potential.[39] In general, the Rh/RhO$_x$-500 catalyst shows more superior performance than other catalysts in alkaline, acid, and neutral solutions. According to literature reports, the comparison of overpotential @ 10 mA cm^{-2} and Tafel slopes for various HER catalysts in 1.0 M PBS indicates that the performance of Rh/RhO$_x$-500 is superior to that of most other catalysts, as shown in Fig. 3e. In addition, the Rh/RhO$_x$-500 catalyst also shows great competitive advantages in alkaline and acidic solutions (Fig. S25†), and the specific data are recorded in Tables S2–S4.† The long-term stability is also very important for electrocatalysts. In Fig. 3f, it can be observed that the LSV curve of Rh/RhO$_x$-500 after 2000 cycles is almost the same as that of the initial curve in 1.0 M PBS and its overpotential only increases 6 mV to deliver a current density of 10 mA cm^{-2}. The chronopotentiometry test was performed at 10 mA cm^{-2}, where the overpotential could be at about 40 mV without significant attenuation after 65 h of operation (Fig. 3g). Moreover, compared with Pt/C whose potential has increased greatly, the durability of Rh/RhO$_x$-500 was tested in 1.0 M KOH and 0.5 M H_2SO_4 and the chronopotentiometry test is performed at 10 mA cm^{-2} (Fig. S26†). No significant decreases in catalytic activity were observed in both tests, which confirmed the excellent stability of the Rh/RhO$_x$-500 catalyst for the HER. The morphology and phase of Rh/RhO$_x$-500 were completely preserved, as confirmed by TEM, XRD, and XPS results (Fig. S27†). It is discovered from XPS spectra of Rh 3d (Fig. S27d†) that the binding energy and content do not change much, proving the stability in electrochemical testing.

OHzS activity of Rh/RhO$_x$-500 in electrolytes with different pH values

Inspired by the excellent catalytic activity and durability of the Rh/RhO$_x$-500 electrode for the HER and HzOR in a neutral medium, we assembled an electrolytic cell and used this electrode as the cathode and anode in a dual electrode system to realize hydrazine assisted hydrogen production.[27] The schematic diagram of the double electrode electrolytic cell and its working principle for the HzOR and HER are shown in Fig. 4a. As shown in Fig. 4b, Rh/RhO$_x$-500 shows higher activity in the

Published on 11 December 2021. Downloaded by Soochow University China on 3/12/2022 11:49:42 AM.

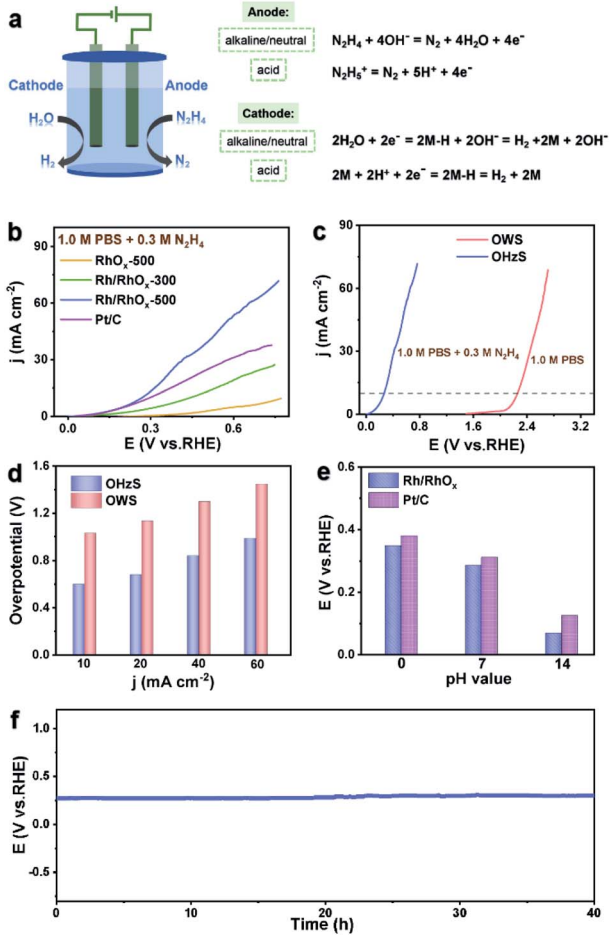

Fig. 4 The electrochemical performance for OHzS. (a) Schematic illustration of the two-electrode electrolyzer (b) LSV curves of different catalysts in 1.0 M PBS/0.3 M N_2H_4. (c) LSV curves for OHzS in 1.0 M PBS/0.3 M N_2H_4 and for OWS in 1.0 M PBS. (d) Comparison of overpotentials at different current densities for OHzS and OWS. (e) Potential comparison of Rh/RhO_x-500 and Pt/C under different pH conditions for OHzS. (f) The chronoamperometry curve for OHzS recorded at 10 mA cm^{-2} current density in 1.0 M KOH/0.3 M N_2H_4.

OHzS cell than other catalysts. It can reach a current density of 10 mA cm^{-2} at a low voltage of 0.268 V, which is much lower than that of Pt/C (0.303 V) and other comparison samples. Additionally, a two electrode system integrating the OER and HER was assembled in a neutral medium for comparison. When H_2 is generated in 1.0 M PBS without N_2H_4, the cathodic reaction is the OER and the cell voltage increases to 2.25 V to reach 10 mA cm^{-2} (Fig. 4c). The OHzS system shown in Fig. 4d can drive current densities of 10, 20, 40, and 60 mA cm^{-2} with an overpotential of 0.598, 0.676, 0.834, and 0.951 V, respectively, which is lower than those of OWS (1.02, 1.13, 1.30 and 1.45 V) at the same current density. Moreover, faradaic efficiency of hydrogen (FE_{H2}) catalyzed by Rh/RhO_x-500 for OHzS determined at a current density of 10 mA cm^{-2} is close to 100% (Fig. S28†), which reveals that the actual H_2 production is consistent with the theoretical results. The above electrocatalytic tests of the Rh/RhO_x-500 catalyst clearly display the huge difference in the two systems and reveal the great economic potential of the catalyst in the hydrazine auxiliary system for commercial H_2 production. In addition, the bifunctional electrocatalyst tested in other media with different pH values only required 0.068 V and 0.348 V in alkaline and acidic electrolytes, respectively, displaying better performance than Pt/C. Potential comparison of Rh/RhO_x-500 and Pt/C under different pH conditions for OHzS is revealed in Fig. 4e and S29a, c.† Especially in alkaline media, ultralow working potentials of 0.068 V and 0.279 V *vs.* RHE are needed to obtain 10 mA cm^{-2} and 100 mA cm^{-2} respectively.

More importantly, Rh/RhO_x-500 showed significant long-term durability with a 32 mV increment after continuous electrolysis for 40 h (Fig. 4f), which proves its potential application value. Besides, the catalyst also exhibits excellent stability in other pH media (Fig. S29b and d†). Compared with other reported catalysts in Table S5,† the OHzS system of Rh/RhO_x-500 also possesses satisfactory advantages.

Promotion mechanisms of Rh/RhO_x for the HzOR and HER

After the previous test, it was found that the performance of the Rh/RhO_x-500 catalyst exceeds that of RhO_x-500, Rh/RhO_x-300, and Pt/C due to the interface between Rh and RhO_x and the nanosheet structure of Rh/RhO_x-500 composites. To disclose the possible origins of the superior bifunctional activity of Rh/RhO_x, DFT calculations were further performed to better understand the HzOR and HER processes, as shown in Fig. 5. The atomic structures of Rh and Rh/RhO_x for the HzOR are

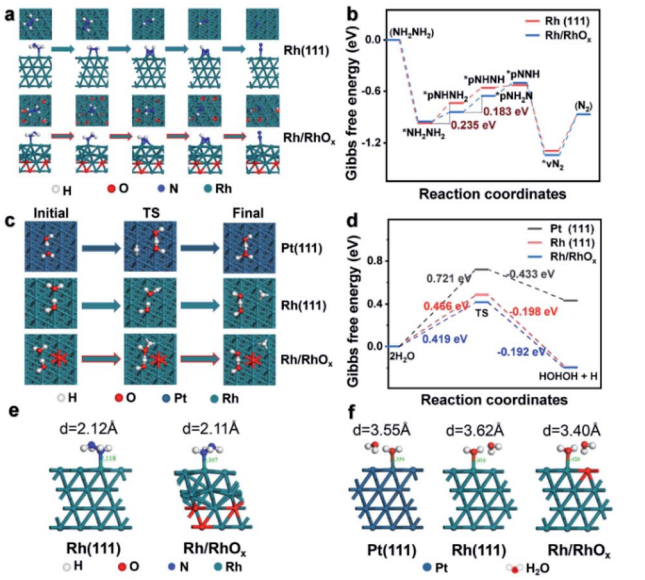

Fig. 5 Theoretical investigation and the proposed mechanism for the HzOR and HER. (a) Top and side views of intermediate configurations for Rh(111) and Rh/RhO_x. (b) Reaction Gibbs free energy diagram of the HzOR in Rh(111) and Rh/RhO_x systems. (c) Top views of configurations for the initial state, transition state (TS), and final state in Pt(111), Rh(111), and Rh/RhO_x systems. (d) Reaction Gibbs free energy diagram for the HER in Pt(111), Rh(111), and Rh/RhO_x systems. (e) Distance between N (NH_2NH_2) and Rh (active site) in Rh(111) and Rh/RhO_x systems for the HzOR. (f) Distance between O (H_2O) and Rh or Rt (active site) in Pt(111), Rh(111), and Rh/RhO_x systems for the HER.

This journal is © The Royal Society of Chemistry 2022

Published on 11 December 2021. Downloaded by Soochow University China on 3/12/2022 11:49:42 AM.

shown in Fig. 5a. For the HzOR, the potential determining step (PDS) on Rh(111) and Rh/RhO_x is different. One is $*NH_2NH_2 \rightarrow *NHNH_2$ on Rh(111) and the other is $*NH_2NH \rightarrow *NH_2N$ on Rh/RhO_x (Fig. 5b). And the formation energy of PDS on Rh(111) and Rh/RhO_x is 0.235 eV and 0.183 eV, respectively (details shown in Table S6†). This significant formation energy drop verifies that the HzOR more easily occurs on Rh/RhO_x than Rh(111), which is consistent with our experimental observations.

The atomic structures of the three systems, including Rh/RhO_x, Rh(111), and Pt(111) for the HER are shown in Fig. 5c. The kinetics of HER is controlled by the water dissociation reaction in the Volmer reaction. Thus the climbing-image nudged elastic band (CI-NEB) is employed to calculate the reaction barrier of water dissociation for the HER, which is the first proton-coupled electron transfer reaction.[40–42] The calculation results show that the barrier of water dissociation on Rh/RhO_x is only 0.419 eV, much lower than those on Pt(0.721 eV) and Rh(0.466 eV) in Fig. 5d (data shown in Table S7†), indicating the lowest energy barrier on Rh/RhO_x advantageous to the HER.

Moreover, when discussing the role of the introduction of the O atom, the change of bond length is further calculated. For the HzOR, the introduced O atom improves the catalytic activity of Rh(111) by shortening the distance between the intermediate $*NH_2NH_2$ and the active center Rh to weaken the N–H bond, which changes the PDS of the reaction and promotes the dehydrogenation of adsorbed $*NH_2NH_2$ on the Rh site. The distance values are shown in Fig. 5e. For the HER, it is observed that the introduced O atom can effectively reduce the energy barrier of water decomposition by shortening the distance between H_2O and the active site and then weakening the H–O bond (Fig. 5f), which is probably beneficial to strengthen the adsorption of H_2O and weaken the desorption of Hads to improve the HER performance. Rh/RhO_x can effectively regulate the distance between the active site and the intermediate so as to change the bond length and strength. Its schematic diagram is shown in Fig. S30,† and this is also the reason why the catalyst shows outstanding performance in a variety of pH environments.

Conclusions

In summary, through reasonable design, Rh/RhO_x-500 with a nanosheet structure was successfully designed to effectively generate hydrogen in electrolytes of different pH values containing hydrazine. Specifically, it can reach a current density of 10 mA cm^{-2} at an overpotential of 39 mV for the HER in 1.0 M PBS and a working potential of 94 mV for the HzOR in 1.0 M PBS/0.3 M N_2H_4, respectively. Moreover, the stability test can reach more than 65 h both for HzOR and HER. It is worth mentioning that the performance of Rh/RhO_x-500 also surpassed that of Pt/C in acidic and alkaline media for the HER and HzOR. Of note, the catalyst performs outstanding in alkaline electrolytes, requiring an ultralow overpotential of 17 mV for the HER in 1.0 M KOH and an ultrasmall working potential of −28 mV for the HzOR in 1.0 M/0.5 M N_2H_4 KOH at 10 mA cm^{-2}. When it comes to hydrazine assisted water electrolyzers, Rh/RhO_x-500 as a dual function electrocatalyst can deliver a current density of 10 mA cm^{-2} for over 40 hours at low voltages of only 0.068, 0.268, and 0.348 V in alkaline, neutral and acidic media, respectively, which is significantly superior to the overall water decomposition performance (OWS). Furthermore, theoretical calculations highlight the significance of the Rh/RhO_x interface on account of the O atom, which would activate the surface Rh and contribute to the HER and HzOR. This work not only provides a deeper understanding of the mechanism of HER and HzOR catalytic activity of layered metal oxides, but also provides a new idea for the design and synthesis of advanced catalytic materials through surface and interface engineering.

Author contributions

Junjun Yang: data curation, visualization. Liang Xu: calculation. Wenxiang Zhu: software. Miao Xie: formal analysis. Fan Liao: writing – review & editing, supervision. Tao Cheng & Zhenhui Kang: project administration, writing – original draft, writing – review & editing. Mingwang Shao: conceptualization, funding acquisition, writing – review & editing, supervision.

Conflicts of interest

There are no conflicts to declare.

Acknowledgements

This work was supported by the National Key Research and Development Program of China (2017YFA0204800), National MCF Energy R&D Program (2018YFE0306105), the National Natural Science Foundation of China (51902217 and 21903058), Collaborative Innovation Center of Suzhou Nano Science & Technology, the Priority Academic Program Development of Jiangsu Higher Education Institutions (PAPD), and the 111 Project and Devices and Postgraduate Research.

References

1 H. Li, M. H. Hu, B. Cao, P. Jing, B. C. Liu, R. Gao, J. Zhang, X. M. Shi and Y. Du, *Small*, 2021, **17**, 2006617.
2 B. B. Jiang, L. L. Yang, F. Liao, M. Q. Sheng, H. Z. Zhao, H. P. Lin and M. W. Shao, *Nano Res.*, 2017, **10**, 1749–1755.
3 G. Feng, F. H. Ning, J. Song, H. F. Shang, K. Zhang, Z. P. Ding, P. Gao, W. S. Chu and D. G. Xia, *J. Am. Chem. Soc.*, 2021, **143**, 17117–17127.
4 Z. W. Zhuang, Y. Wang, C. Q. Xu, S. J. Liu, C. Chen, Q. Peng, Z. B. Zhuang, H. Xiao, Y. Pan, S. Q. Lu, R. Yu, W. C. Cheong, X. Cao, K. L. Wu, K. Sun, Y. Wang, D. S. Wang and Y. D. Li, *Nat. Commun.*, 2019, **10**, 4875.
5 Q. Xue, H. Huang, J. Y. Zhu, Y. Zhao, F. M. Li, P. Chen and Y. Chen, *Appl. Catal. B*, 2020, **278**, 119269.
6 Q. Xue, X. Y. Bai, Y. Zhao, Y. N. Li, T. J. Wang, H. Y. Sun, F. M. Li, P. Chen, P. Jin, S. B. Yin and Y. Chen, *J. Energy Chem.*, 2022, **65**, 94–102.

Published on 11 December 2021. Downloaded by Soochow University China on 3/12/2022 11:49:42 AM.

7 T. J. Wang, H. Y. Sun, Q. Xue, M. J. Zhang, F. M. Li, X. L. Tian, P. Chen, S. B. Yin and Y. Chen, *Sci. Bull.*, 2021, **66**, 2079–2089.
8 Q. Xue, Y. Zhao, J. Y. Zhu, Y. Ding, T. J. Wang, H. Y. Sun, F. M. Li, P. Chen, P. J. Jin, S. B. Yin and Y. Chen, *J. Mater. Chem. A*, 2021, **9**, 8444–8451.
9 M. Zhang, Z. Q. Wang, Z. Y. Duan, S. Q. Wang, Y. Xu, X. N. Li, L. Wang and H. J. Wang, *J. Mater. Chem. A*, 2021, **9**, 18323–18328.
10 F. He, N. N. Xia, Y. Zheng, Y. X. Zhang, H. L. Fan, D. Ma, Q. H. Liu and X. Hu, *ACS Appl. Mater. Interfaces*, 2021, **13**, 8488–8496.
11 J. Y. Zhang, H. M. Wang, Y. F. Tian, Y. Yan, Q. Xue, T. He, H. F. Liu, C. D. Wang, Y. Chen and B. Y. Xia, *Angew. Chem., Int. Ed.*, 2018, **57**, 7649–7653.
12 L. Wang, J. H. Cao, X. D. Cheng, Q. Z. Dai, B. Yang, Z. J. Li, M. A. Younis, L. C. Lei, Y. Hu and K. Ostrikov, *ACS Sustainable Chem. Eng.*, 2019, **7**, 10044–10051.
13 N. Jia, Y. P. Liu, L. Wang, P. Chen, X. B. Chen, Z. W. An and Y. Chen, *ACS Appl. Mater. Interfaces*, 2019, **11**, 35039–35049.
14 Z. Y. Wang, L. Xu, F. Z. Huang, L. B. Qu, J. T. Li, K. A. Owusu, Z. Liu, Z. F. Lin, B. H. Xiang, X. Liu, K. N. Zhao, X. B. Liao, W. Yang, Y. B. Cheng and L. Q. Mai, *Adv. Energy Mater.*, 2019, **9**, 1900390.
15 Y. Li, Y. Zhao, F. M. Li, Z. Y. Dang and P. Q. Gao, *ACS Appl. Mater. Interfaces*, 2021, **13**, 34457–34467.
16 S. N. Hu, Y. Tan, C. Q. Feng, H. M. Wu, J. J. Zhang and H. Mei, *J. Power Sources*, 2020, **453**, 227872.
17 W. H. Guo, K. X. Zhang, Z. B. Liang, R. Q. Zou and Q. Xu, *Chem. Soc. Rev.*, 2019, **48**, 5658–5716.
18 Y. Zhao, N. Jia, X. R. Wu, F. M. Li, P. Chen, P. J. Jin, S. W. Yin and Y. Chen, *Appl. Catal. B*, 2020, **270**, 118880.
19 Y. Liu, J. H. Zhang, Y. P. Li, Q. Z. Qian, Z. Y. Li and G. Q. Zhang, *Adv. Funct. Mater.*, 2021, **31**, 2103673.
20 Y. P. Li, J. H. Zhang, Y. Liu, Q. Z. Qian, Z. Y. Li, Y. Zhu and G. Q. Zhang, *Sci. Adv.*, 2020, **6**, eabb4197.
21 C. X. Zhang, H. X. Liu, Y. F. Liu, X. J. Liu, Y. Y. Mi, R. J. Guo, J. Q. Sun, H. H. Bao, J. He, Y. Qiu, J. Q. Ren, X. J. Yang, J. Luo and G. Z. Hu, *Small Methods*, 2020, **4**, 2000208.
22 G. Q. Liu, Z. T. Sun, X. Zhang, H. J. Wang, G. Z. Wang, X. J. Wu, H. M. Zhang and H. J. Zhao, *J. Mater. Chem. A*, 2018, **6**, 19201–19209.
23 M. K. Kundu, R. Mishra, T. Bhowmik and S. Barman, *J. Mater. Chem. A*, 2018, **6**, 23531.
24 A. R. Puigdollers, P. Schlexer, S. Tosoni and G. Pacchioni, *ACS Catal.*, 2017, **7**, 6493–6513.
25 M. Barua, M. M. Ayyub, P. Vishnoi, K. Pramodaa and C. N. R. Rao, *J. Mater. Chem. A*, 2019, **7**, 22500–22506.
26 U. Holzwarth and N. Gibson, *Nat. Nanotechnol.*, 2011, **6**, 534.
27 Z. Novotny, B. Tobler, L. Artiglia, M. Fischer, M. Schreck, J. Raabe and J. Osterwalder, *J. Phys. Chem. Lett.*, 2020, **11**, 3601–3607.
28 Z. Li, Y. Feng, Y. L. Liang, C. Q. Cheng, C. K. Dong, H. Liu and X. W. Du, *Adv. Mater.*, 2020, **32**, 1908521.
29 S. X. Bai, M. Xie, T. Cheng, K. L. Cao, Y. Xu and X. Q. Huang, *Nano Energy*, 2020, **78**, 105224.
30 K. Y. Zhu, J. Y. Chen, W. J. Wang, J. W. Liao, J. C. Dong, M. O. L. Chee, N. Wang, P. Dong, P. M. Ajayan, S. P. Gao, J. F. Shen and M. X. Ye, *Adv. Funct. Mater.*, 2020, **30**, 2003556.
31 L. H. Wang, X. L. Teng, Y. F. Qin and Q. Li, *Ceram. Int.*, 2021, **47**, 5739–5746.
32 T. R. Gengenbach, G. H. Major, M. R. Linford and C. D. Easton, *J. Vac. Sci. Technol., A*, 2021, **39**, 013204.
33 X. F. Lu, L. Yu and X. W. Lou, *Sci. Adv.*, 2019, **5**, eaav6009.
34 Y. M. Sun, Z. Q. Xue, Q. L. Liu, Y. L. Jia, Y. L. Li, K. Liu, Y. Y. Lin, M. Liu, G. Q. Li and C. Y. Su, *Nat. Commun.*, 2021, **12**, 1369.
35 F. Luo, Q. Zhang, X. X. Yu, S. L. Xiao, Y. Ling, H. Hu, L. Guo, Z. H. Yang, L. Huang, W. W. Cai and H. S. Cheng, *Angew. Chem., Int. Ed.*, 2018, **57**, 14862–14867.
36 Q. Z. Qian, J. H. Zhang, J. M. Li, Y. P. Li, X. Jin, Y. Zhu, Y. Liu, Z. Li, A. E. Harairy, C. Xiao, G. Q. Zhang and Y. Xie, *Angew. Chem., Int. Ed.*, 2021, **60**, 5984–5993.
37 B. B. Jiang, F. Liao, Y. Y. Sun, Y. F. Cheng and M. W. Shao, *Nanoscale*, 2017, **9**, 10138–10144.
38 H. X. Shi, L. B. Liu, Y. D. Shi, F. Liao, Y. Z. Li and M. W. Shao, *Int. J. Hydrogen Energy*, 2019, **44**, 11817–11823.
39 L. Zhu, H. P. Lin, Y. Y. Li, F. Liao, Y. Lifshitz, M. Q. Sheng, S. T. Lee and M. W. Shao, *Nat. Commun.*, 2016, **7**, 12272.
40 G. Henkelman and H. Jónsson, *J. Chem. Phys.*, 2000, **113**, 9978–9985.
41 G. Henkelman, B. P. Uberuaga and H. Jónsson, *J. Chem. Phys.*, 2000, **113**, 9901–9904.
42 J. Durst, A. Siebel, C. Simon, F. Hasché, J. Herranz and H. A. Gasteiger, *Energy Environ. Sci.*, 2014, **7**, 2255–2260.

 This journal is © The Royal Society of Chemistry 2022